Optics Letters

Machine-learning-assisted omnidirectional bending sensor based on a cascaded asymmetric dual-core PCF sensor

Bingsen Huang,[1] Xinzhi Sheng,[1] Jiaqi Cao,[2] Haoqiang Jia,[2] Wei Gao,[2] Shuai Gu,[2] Xin Wang,[2] Paul K Chu,[3] and Shuqin Lou[2,*]

[1]School of Science, Beijing Jiaotong University, Beijing 100044, China
[2]Key Laboratory of Communication and Information Systems, Beijing Municipal Commission of Education, School of Electronic and Information Engineering, Beijing Jiaotong University, Beijing 100044, China
[3]Department of Physics, Department of Materials Science and Engineering, and Department of Biomedical Engineering, City University of Hong Kong, Tat Chee Avenue, Kowloon, Hong Kong, China
*shqlou@bjtu.edu.cn

Received 8 June 2023; revised 26 July 2023; accepted 30 July 2023; posted 14 August 2023; published 18 September 2023

An omnidirectional bending sensor comprising cascaded asymmetric dual-core photonic crystal fibers (ADCPCFs) is designed and demonstrated experimentally. Upon cascading and splicing two ADCPCFs at a lateral rotation angle, the transmission spectrum of the sensor becomes highly dependent on the bending direction. Machine learning (ML) is employed to predict the curvature and bending orientation of the bending sensor for the first time, to the best of our knowledge. The experimental results demonstrate that the ADCPCF sensor used in combination with machine learning can predict the curvature and omnidirectional bending orientation within 360° without requiring any post-processing fabrication steps. The prediction accuracy is 99.85% with a mean absolute error (MAE) of 2.7° for bending direction measurement and 98.08% with an MAE of 0.03 m^{-1} for the curvature measurement. This promising strategy utilizes the global features (full spectra) in combination with machine learning to overcome the dependence of the sensor on high-quality transmission spectra, the wavelength range, and a special wavelength dip in the conventional dip tracking method. This excellent omnidirectional bending sensor has large potential for structural health monitoring, robotic arms, medical instruments, and wearable devices.

https://doi.org/10.1364/OL.497509

Information pertaining to bending/curvature is crucial to the measurement of mechanical bending, structural health monitoring, human posture detection, and robotics. Optical fibers are immune to electromagnetic interference, and their small size and small weight render them excellent to use in bending sensors. Generally, optical fibers with non-cylindrical structures are used to construct bending sensors to detect two opposite bending directions in a plane [1]. Although two-dimensional vector bending sensors based on multi-core fiber (MCF) with fiber Bragg gratings (FBGs) inscribed in the inner cores have been reported [2,3], it is still challenging to inscribe high-quality FBGs efficiently on each core of the MCF. Moreover, these sensors require accurate alignment techniques as well as fan-in/out devices, thus making the sensing system and manufacturing complex. In addition, the traditional two-dimensional vector bending sensor usually demands a reconstructing algorithm based on the measured signal of each core and the orthogonal relationship between them (by means of trigonometric calculation), thereby making it more complicated and inefficient. In order to simplify the reconstruction process, Yang *et al.* proposed a two-dimensional vector bending sensor based on a hole-assisted three-core fiber coupler in 2022 [4]. The dip tracking and coordinate calibration method is utilized to reconstruct the bending direction and curvature. However, there are some blind areas when detecting the bending direction. In 2023, Xu *et al.* inscribed orthogonal single-mode helical Bragg gratings into the fiber cladding for vector bending measurements [5]. Both the orientation and amplitude of the bending vector could be reconstructed by measuring the Bragg wavelength shifts. However, these schemes are based on the dip tracking approach, in which the bending direction and curvature are determined by the linear response of the wavelength dips. Hence, most of the information in the sensor spectra is lost because the dip tracking method only focuses on one or several wavelength dips. These feature dips may be distorted, become rough, disappear, or shift beyond the wavelength window when the sensor is subjected to a large change, consequently causing ambiguities when identifying the sensing dips [6]. Furthermore, the sensor visibility or contrast decreases when the sensor length increases. These constraints have hampered the development of omnidirectional bending sensors based on the dip-tracking method.

Machine learning (ML) has recently attracted wide interest in the field of optical fiber sensing. It can be implemented to obtain information about the mapping relationship between the complex optical spectra and measured entities for fiber interferometers [7]. ML can make full use of the information in the full spectra rather than only a particular wavelength dip, consequently overcoming the limitation of the traditional fitting

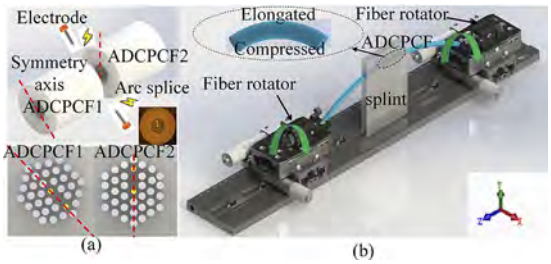

Fig. 1. (a) Schematic diagram of the cascaded splicing of the ADCPCFs, with the two ADCPCFs spliced at an intersection angle. The inset shows cross sections of the fabricated ADCPCFs (the yellow dots at the center of the PCFs represent the fiber cores). (b) Schematic diagram of the directional bending setup, with the inset at the top showing how the sensor is compressed or elongated.

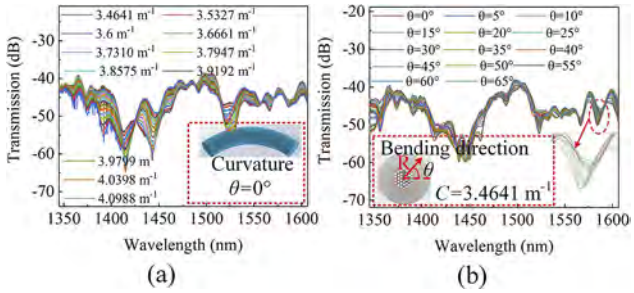

Fig. 2. Transmission spectra of the sensor at different settings of (a) curvature (at $\theta = 0°$) and (b) bending direction (at $C = 3.4641\ \mathrm{m}^{-1}$).

method. This offers the opportunity to realize omnidirectional bending, but, up to now, experiments on bending direction measurements using machine learning methods have seldom been reported. Li *et al*. have proposed a deep-learning-based curvature sensor based on specklegram detection [8], and Zhu *et al*. have described an ML-boosted vector bending sensor [9]. In addition, Cui *et al*. have discussed a random-forest-assisted vector displacement sensor [10], and Sun *et al*. have proposed a directional position sensor based on multimode interference imaging and ML [11]. However, none of these sensors can simultaneously achieve curvature and omnidirectional bending sensing.

In this Letter, we report a machine-learning-assisted omnidirectional bending sensor based on cascaded asymmetric dual-core photonic crystal fibers (ADCPCFs). The cascaded ADCPCFs are spliced such that there is a lateral rotation angle between their symmetry axes; in this way, the refractive indices (RIs) of the two cores are modulated differently when the fiber is bent at an arbitrary angle. A total of 1,095 original transmission spectra are acquired experimentally from the ADCPCF sensor, and a backpropagation neural network (BPNN) model is employed to predict the bending direction and curvature. The experimental results demonstrate that the well-trained BPNN model not only predicts the bending direction for an arbitrary orientation within 360° with a high accuracy of 99.85%, but it also yields small average relative errors of 2.53% and 0.67% in the prediction of the bending direction and curvature, respectively. The strategy is easy to implement and does not require complicated alignment systems and complex orientation reconstructing algorithms, boding well for low-cost and high-accuracy omnidirectional bending detection.

In the omnidirectional bending sensor, two segments of ADCPCF that are spliced such that there is a lateral rotation angle between their symmetry axes, as shown in Fig. 1(a). The ADCPCF shown in the inset in Fig. 1(a) is a silica PCF with one core arranged at the center and the other core placed off the axis. The outer diameter of the ADCPCF is 125 μm, the air hole pitch is 7.5 μm, and the diameter of the air hole is 5.25 μm. The diameter of the germanium-doped core is 3 μm and the RI difference between the germanium-doped core and pure silica is 0.003. The 3-cm-long and 2-cm-long ADCPCFs are spliced such that there is a lateral rotation angle between the symmetry axes of the ADCPCFs (this is illustrated in detail in Ref. [1]). In this way, the RIs of the two cores are modulated differently when the fiber is bent along an arbitrary orientation. As described in our previous papers [1], owing to the asymmetrical distribution of the twin cores in the ADCPCF, the bending response of the sensor depends strongly on the bending direction. In our design, the two ADCPCFs are spliced at a lateral rotation angle so that the symmetry of the bending sensor is broken. As demonstrated previously [1], the bending response of the ADCPCF-based sensor depends strongly on the bending direction.

A broadband light source (BLS, SC-5-FC, YSL) serves as the input light source, and the transmission spectra are acquired on an optical spectrum analyzer (OSA, MS9740A, Anritsu). The sensor is mounted on two optical fiber rotation modules fixed to two translation stages, as shown in Fig. 1(b). The sensor is placed between two splints to ensure that the bending direction is parallel to the y axis and the sensor bends along the y axis when the translation stage moves along the z axis. By rotating the two fiber rotators at the same time, the bending characteristics for each optical fiber orientation angle are monitored in steps of 5° between 0° and 360°. The initial distance between the two stages is 100 mm and the initial curvature is set to $3.4641\ \mathrm{m}^{-1}$ to ensure that the sensor does not experience residual distortion. The bending characteristics are determined by moving the linear translation stage in steps of 20 μm. In each curvature step, the transmission spectrum is collected and bending characterization is performed for each bending orientation by simultaneously adjusting the two fiber rotation modules in steps of 5° from 0 to 360°. Figures 2(a) and 2(b) display representative transmission spectra of the sensor for different settings of curvature and bending direction, respectively. The complex spectra are the result of mode interference [7]. The mechanism for the interference spectrum of the sensor was illustrated in our previous paper [1]. Multiple fringe troughs, which can be regarded as optical features of the BPNN and can potentially be utilized for sensing, can be observed in the spectra. Instead of focusing on one or several particular fringe dips (shifts in the dip wavelength or changes in its magnitude), the machine-learning-based analysis directly learns the relevant features from the entire spectra and subsequently achieves one-to-one mapping between the original spectra and the bending direction and curvature.

The BPNN model used to resolve the ADCPCF spectra is schematically illustrated in Fig. 3. The BPNN model used in this work is configured with one input layer, two hidden layers, and one output layer. These layers include 2,500, 10, 10, and 2 nodes after empirical validation. The activation functions used for the hidden layers and output layer are sigmoid and linear, respectively. The original spectral data are sent to the input layer directly. The output layer maps the feature vectors to the final

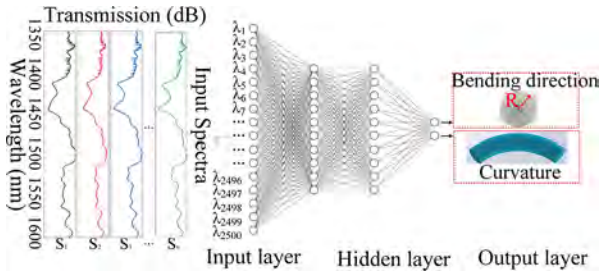

Fig. 3. Spectra and corresponding labels used to train the BPNN. S_1 represents spectrum 1, S_N represents spectrum N, and N = 1,095.

output related to the predicted values of the bending direction and curvature. The mean square error (MSE) is the loss function, as defined in the following:

$$\mathrm{MSE} = \frac{1}{n}\sum_{i=1}^{n}(y_i - \hat{y}_i)^2, \tag{1}$$

where n is the number of samples, $\hat{y}_i$ is the predicted value from the BPNN model, and y_i is the actual experimental value. The coefficient of determination R^2 is utilized as the evaluation function; this can be expressed as

$$R^2 = 1 - \frac{\Sigma_i(y_i - \hat{y}_i)^2}{\Sigma_i(y_i - \bar{y})^2}, \tag{2}$$

where $\bar{y}$ is the average of the true value, and R^2 can be regarded as the prediction accuracy of the model. The closer that R^2 approaches 1, the more accurate the optimized result. The mean absolute error (MAE) is chosen to evaluate the measurement error, and it is calculated as follows:

$$\mathrm{MAE} = \frac{1}{n}\sum_{i=1}^{n}\left|\hat{y}_i - y_i\right|. \tag{3}$$

The standard Adam optimizer is adopted by the model to optimize the learning rate, and the initial value is 0.01. The BPNN model is trained and validated in MATLAB 2021a on a computer with Intel i5 9600 K 6-core processors.

According to the above analysis, there is a one-to-one mapping relationship between the original spectra and the bending direction and curvature. To demonstrate omnidirectional bending and curvature recognition, a set of mapping relations between the testing status and output spectra are constructed in the experiment. The dataset is collected as follows. The bending direction is increased from 0° to 360° in steps of 5°, giving rise to 73 bending directions, and about 15 curvatures are collected for each bending direction. Finally, a total of 1,095 spectra are input into the model sequence, with 2,500 sample points for each group of data. Among them, 70% of the samples are used as the training dataset, and the rest are used as the testing dataset. Once trained, the BPNN can predict the bending direction and curvature buried in the interference spectra.

Figure 4 presents a scatterplot of the predicted values and actual values of the bending direction and curvature. Each circle corresponds to a single data point, i.e., a single measurement for an applied bending direction and curvature. In the ideal model, these data points should be exactly aligned along the y = x line, as indicated by the red line. The data points in Figs. 4(a) and 4(c) are the dataset used to train the BPNN model. The MSE

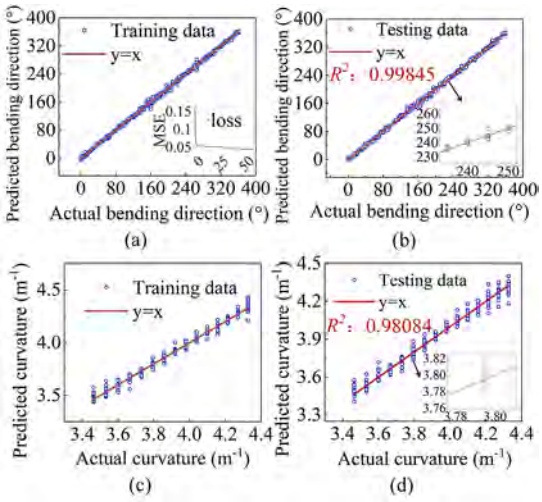

Fig. 4. Predicted bending direction obtained using the (a) training dataset and (b) testing dataset versus the set bending direction for the ADCPCF sensor. Predicted curvature obtained using the (c) training dataset and (d) testing dataset versus the set curvature for the ADCPCF sensor. The inset in (a) shows a plot of the MSE obtained versus epochs during the training process. The insets in (b) and (d) are enlarged views for a bending direction of 245° and curvature of 3.79 m^{-1}.

as a function of the training epoch during the training process is plotted in the inset of Fig. 4(a). The MSE decreases rapidly initially but gradually stabilizes after epoch 50. As shown in Figs. 4(a) and 4(c) for the training dataset (70% of the 1,095 spectral data samples), the trained BPNN model successfully maps the measured original spectra to the corresponding bending direction and curvature, indicating that the model can extract the relevant features from the spectra and memorize the complex mapping between the spectral response and corresponding testing status (bending direction and curvature). Figures 4(b) and 4(d) show a scatterplot of the test dataset that is not seen by the BPNN model in the training process. The predicted and actual values of the bending direction and curvature are close, showing small errors and high correlation coefficients of 0.99845 and 0.98084, revealing that the trained BPNN model can predict the bending direction and curvature effectively.

In order to analyze the error of each testing sample more accurately, numerical statistics is performed to determine the distribution of the predicted errors. Figure 5(a) shows an error histogram of the bending direction for the testing data samples predicted by the BPNN model. 322 samples are predicted with an error of less than 10° across the whole range of 360°, corresponding to 98.17% of the 328 testing data samples. The MAE of the testing points is 2.7° and the maximum measurement error of these points is 15°, with the BPNN model gauging the bending direction of 135° to be 150° (the probability of occurrence in the test points is 0.31%). Figure 5(b) shows a histogram of the relative errors of the bending direction measurement for 328 testing data samples predicted by the BPNN model. Approximately 96.03% of the data samples are predicted with a relative error of less than 10% across the whole range of 360°. The average relative error of these points is 2.53%. There is only one sample point with a relative error of 40%, as shown in Fig. 5(b). By further analyzing the data at this point, it is found that the BPNN model regards the bending direction of 10° as

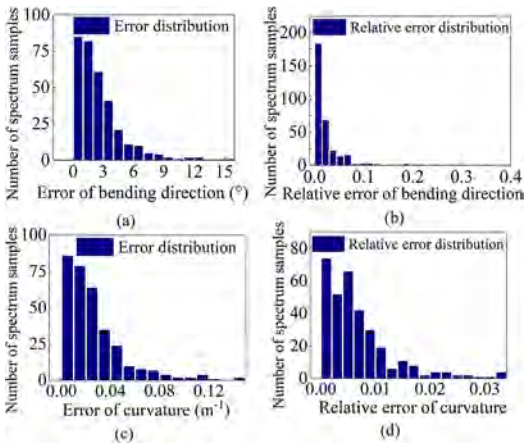

Fig. 5. Histograms of (a) the error and (b) the relative error between the predicted and set bending directions. Histograms of (c) the error and (d) the relative error between the predicted and set curvatures.

6°. Considering that this error occurs in the small angle assessment and the overall probability of occurrence is only 0.31%, the predicted results are highly reliable. Figure 5(c) shows a histogram of the curvature errors for the testing data samples. 319 samples are predicted with an error of less than 0.1 m^{-1}, translating to 97.26% of the testing data. The average relative error of the curvature measurement is 0.67%, and the MAE of the curvature measurement is 0.03 m^{-1}. Figure 5(d) displays a histogram of the relative errors of curvature measurement for a total of 328 testing data samples predicted by the BPNN model. Approximately 94.52% of the data samples are predicted with a relative error of less than 2%. The maximum predicted error is 0.1433 m^{-1} (4.3267 m^{-1} predicted as 4.1834 m^{-1}), corresponding to a relative error of 3.31%, indicating a relatively small prediction error.

An additional experiment is performed to demonstrate the feasibility of the BPNN model when using low-resolution interrogation hardware. The results are given in Supplement 1. Figure S1 and Table S1 in Supplement 1 indicate that the proposed strategy is capable of reducing the cost of the interrogation hardware by lowering the resolution while retaining the measurement accuracy. It should be noted that it is challenging, if not impossible, to maintain the same accuracy while reducing the resolution if the conventional dip tracking method is employed. The transmission spectrum with a resolution of 1.1 nm is taken as an example, as shown in Fig. S2(a). As the spectrum becomes sparse, the wavelength dip becomes flat, resulting in an ambiguity of 1.1 nm for the dip tracking method. This produces a measurement error of 12.2° (the sensitivity is 0.09 nm/° in the inset). On the other hand, while extracting the dip wavelength, it is found that the number of points used to fit the smooth signal is critically important and can cause ambiguity. For example, the original spectrum with many ripples collected in the experiment is shown in the inset in Fig. S2(b). A smooth curve fit is applied to find the dip wavelength. The determined dip wavelengths are plotted against the number of fitted points in Fig. S2(b). The dip wavelengths vary by up to 1.56 nm when different numbers of points are used, corresponding to a variation of 17°. Table S2 in Supplement 1 shows that our strategy delivers a comparable performance in detecting the bending direction (2.53%) and a better performance (0.67%) in curvature measurement than previous works [2,12].

In summary, a novel machine-learning-assisted omnidirectional bending sensor based on a cascaded ADCPCF sensor has been designed and analyzed. Two cascaded ADCPCFs are spliced such that there is a lateral rotation angle between their symmetry axes. Because of the asymmetrical distribution of the twin cores in the ADCPCF, the cascade splicing of the two ADCPCFs enables the sensor to respond depending on the arbitrary bending direction. In addition, the BPNN model makes full use of the interference spectra instead of performing traditional dip wavelength tracking and complicated orientation reconstruction. The spectral feature changes are accumulated to directly and statistically learn the relationship between the complex spectra and sensor status (bending direction and curvature), consequently helping to eliminate the dependence on a high-quality transmission spectrum, the wavelength range, and a special wavelength dip. The MAE values of the bending direction and curvature are 2.7° and 0.03 m^{-1}, with average relative errors of 2.53% and 0.67%, respectively, indicating excellent performance in actual measurements compared to the traditional wavelength tracking and orientation reconstruction method. Last but not least, the new design is easy to implement because expensive lasers, precise alignment techniques, as well as fan-in/out devices are not required. The ADCPCF sensor used in combination with machine learning algorithms is promising for realizing omnidirectional bending and curvature recognition and has high potential in structural health monitoring, robotic arms, and medical instruments.

Funding. National Natural Science Foundation of China (12174022); Beijing Municipal Natural Science Foundation (1232028); City University of Hong Kong (DON-RMG 9229021, 9220061).

Disclosures. The authors declare no conflicts of interest.

Data availability. Data underlying the results presented in this paper are not publicly available at this time but may be obtained from the authors upon reasonable request.

Supplemental document. See Supplement 1 for supporting content.

REFERENCES

1. Z. Tang, S. Lou, X. Wang, W. Zhang, S. Yan, and Z. Xing, IEEE Sens. J. **19**, 4062 (2019).
2. M. Hou, K. Yang, J. He, X. Xu, S. Ju, K. Guo, and Y. Wang, Opt. Express **26**, 23770 (2018).
3. W. Bao, N. Sahoo, Z. Sun, C. Wang, S. Liu, Y. Wang, and L. Zhang, Opt. Express **28**, 26461 (2020).
4. J. Yang, F. Zou, C. Guan, P. Ye, S. Gao, Z. Zhu, P. Li, J. Shi, J. Yang, and L. Yuan, Opt. Lett. **47**, 5953 (2022).
5. B. Xu, J. He, X. Xu, C. Liao, X. Weng, L. Liu, J. Qu, and Y. Wang, Opt. Lett. **48**, 452 (2023).
6. F. Wang, Y. Liu, Y. Lu, L. Zhang, J. Ma, L. Wang, and W. Sun, Opt. Lett. **43**, 5355 (2018).
7. L. V. Nguyen, C. C. Nguyen, G. Carneiro, H. Ebendorff-Heidepriem, and S. C. Warren-Smith, Photonics Res. **9**, B109 (2021).
8. G. Li, Y. Liu, Q. Qin, X. Zou, M. Wang, and F. Yan, Opt. Laser Technol. **149**, 107873 (2022).
9. C. Zhu and J. Huang, Opt. Express **30**, 24553 (2022).
10. J. Cui, H. Luo, J. Lu, X. Cheng, and H.-Y. Tam, Opt. Express **29**, 15852 (2021).
11. K. Sun, Z. Ding, and Z. Zhang, Appl. Opt. **59**, 5745 (2020).
12. R. Oliveira, M. Cardoso, and A. M. Rocha, Opt. Express **30**, 2230 (2022).